

(n, m) Structural Assignments and Chirality Dependence in Single-Wall Carbon Nanotube Raman Scattering

Zhonghua Yu and Louis E. Brus*

Department of Chemistry, Columbia University, New York, New York 10027

Received: March 6, 2001; In Final Form: May 2, 2001

Raman spectra were obtained from thin bundles containing just a few single-wall carbon nanotubes (SWNTs). These spectra exhibit new characteristics absent in the ensemble Raman measurements. A large variation in the radial breathing mode (RBM) Stokes to anti-Stokes Raman intensity ratio was observed for different metallic tubes and can be understood with a simple resonant Raman analysis. An (n, m) structural assignment for many tubes at 632 nm laser excitation was tentatively achieved on the basis of the RBM frequency and the Stokes to anti-Stokes Raman ratio. The (9, 9) armchair tube fits the simple model poorly. The varying relative intensities of different components observed in the tangential G-band Raman modes provide convincing evidence for a recently predicted chirality dependence of Raman scattering. A new Raman feature at 1417 cm^{-1} was assigned to achiral tubes.

Introduction

Single-wall carbon nanotubes (SWNTs) have been the focus of intense research^{1,2} since their discovery in 1991.^{3,4} Raman scattering has been proven to be valuable as a remote, contactless method of sample characterization and as a method for studying the one-dimensional (1D) electronic and vibrational properties of SWNTs.⁵ Raman spectroscopy of ensembles exhibits the radial breathing mode (RBM) at $\sim 200 \text{ cm}^{-1}$ and the tangential C–C stretching G-band modes near 1600 cm^{-1} .⁵ RBM properties have been well established; the frequency depends sensitively on the diameter of a nanotube but not on its chirality.⁶ The G-band Raman spectra are complicated and severely compromised by ensemble averaging. In ensembles, perhaps 50 different (n, m) structural types are simultaneously present. Three different symmetry G-band vibrational modes, A_1 , E_1 , and E_2 , are involved. For a general chiral tube, each symmetry mode splits into a transverse optical mode (TO) vibration and a longitudinal optical mode (LO) vibration because of the zone-folding and curvature effects; their frequencies are predicted to be less diameter-sensitive.^{1,6} Moreover, the G-band scattering from metallic tubes shows an asymmetrically broadened Fano line shape at $\sim 1540 \text{ cm}^{-1}$.^{5,7} Very recently, a polarized Raman study was performed on aligned SWNTs, and the symmetry properties of the G-band modes in semiconducting tubes were determined accordingly.⁸ The relative Raman intensities of the different components in the G-band are predicted to depend on the chirality of a tube.^{8–10} Experimentally, however, little evidence¹⁰ has been reported for this chirality dependence.

Raman scattering in SWNTs is, both theoretically¹¹ and experimentally,⁵ resonantly enhanced at the sharp, molecular-electronic-state-like interband transitions between the van Hove singularities (vHs) in the 1D electronic density of states (DOS).^{1,12} A trigonal warping effect in the energy dispersion relations splits the vHs into two peaks for metallic nanotubes,¹³ depending on chirality. Metallic zigzag nanotubes exhibit a

maximum splitting, while no splitting is expected for armchair nanotubes or semiconducting nanotubes.¹³ For example, in the (18, 0) zigzag tube (diameter $d_t = 1.4 \text{ nm}$), the first interband transition energy $E^1(d_t)$ is predicted to be split by 0.18 eV. This peak splitting should create interesting interference in the resonance Raman scattering.^{14,15}

Early Raman studies^{5,16,17} focused on ensemble samples, in which the measured Raman spectra were averaged over many different structures. Raman measurements on single thick bundles of perhaps 10^2 SWNTs were performed recently,^{8,18,19} but the data did not differ very much from the ensemble data. Both Duesberg et al.²⁰ and Jorio et al.²¹ have recently obtained spectra from single thin bundles and tubes. Jorio et al.²¹ assigned the (n, m) structure for the observed RBM Raman peaks between 144 and 174 cm^{-1} (diameter $\sim 1.43\text{--}1.72 \text{ nm}$) on the basis of the measured RBM Stokes Raman intensity from one tube to the next. The SWNTs were laid down on a substrate, which created strong background scattering, hindering the observation of weak Raman features and the precise metallic Fano Raman line shape analysis.

We use a simple method to measure Raman scattering with low background from suspending thin bundles of SWNTs with smaller diameters ($\sim 1.2 \text{ nm}$). Our results provide strong experimental evidence for the importance of trigonal warping¹³ and chirality^{8–10} in Raman scattering and also help interpret the complex Raman spectra of ensemble samples. In addition, an approximate (n, m) structural assignment in metallic tubes is achieved on the basis of the relative Stokes to anti-Stokes RBM Raman intensities, with the aid of a simplified resonance Raman calculation.

Experimental Section

Raman scattering measurements were performed on suspending individual SWNT bundles in the backscattering configuration using an inverted optical microscope.^{18,19} The SWNT material (Tubes@Rice, diameter distribution $\sim 1.05\text{--}1.5 \text{ nm}$, peaked at 1.2 nm) dispersed in aqueous surfactant²² was filtered through a membrane filter, leaving a mat of SWNTs (bucky-paper) on the membrane. The buckypaper was removed and

* E-mail: brus@chem.columbia.edu.

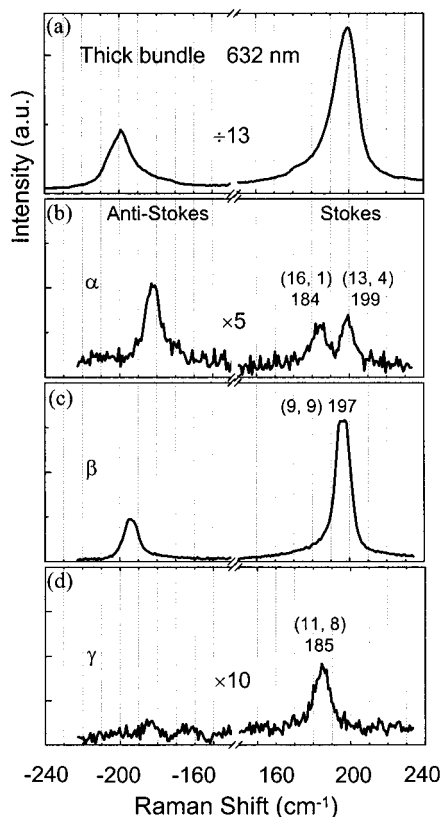


Figure 1. Radial breathing mode Stokes (shown as positive Raman shift) and anti-Stokes (shown as negative Raman shift) Raman spectra of a thick bundle (a) and three thin bundles of SWNTs (b–d). The excitation wavelength is 632 nm. The corresponding G-band Raman spectra for the thin bundles are shown in Figure 5a, b, and e, respectively. Also shown are the (n, m) structural assignments for the thin bundle RBM peaks.

heated in flowing Ar at 400 °C to drive off adsorbed species that otherwise affect the Fano line shapes.^{18,19} After pulling and tearing the buckypaper, suspended thick single bundles were observed to protrude from the buckypaper edge with dark field illumination. Nearly invisible thin bundles exist at the end of the protruding thick bundles; they can be located by focusing a laser beam beyond the bundle end and observing weak Rayleigh scattering light in the microscope by eye. This Rayleigh scattering was constantly monitored and the sample position adjusted relative to the laser focus spot to compensate for thermal drift during data acquisition over ~1 h. Laser excitation at 457 and 442 nm, polarized along the bundle axis, was used to resonantly select the semiconducting tubes. Randomly polarized 632 nm laser light was used to mainly excite the metallic tubes in the bundle. Both RBM Stokes and anti-Stokes Raman scattering could be measured simultaneously with 632 nm excitation; typical excitation intensity is ~100–200 kW/cm².

Results and Discussion

RBM Raman Scattering. Figure 1 displays Stokes and anti-Stokes RBM Raman spectra from three thin bundles, α , β , and γ , with 632 nm excitation (Figure 1b–d) along with a typical spectrum from a thick bundle (Figure 1a). The thick bundle RBM spectrum shows a broad peak at ~199 cm⁻¹, with a line width (fwhm) of ~18 cm⁻¹. The thin bundle spectra show narrower RBM features at various peak positions, with a typical line width (fwhm) of 9 cm⁻¹, comparable to the reported natural line widths of 5–10 cm⁻¹ at room tempera-

ture.^{21,23} Also, in our measurements, the thin bundle Raman signal is typically 10–100 times weaker than the prior thick bundle Raman signal.^{18,19} As a thick bundle contains a few hundred individual tubes,²⁴ only a few tubes are present in the thin bundles.

Varying relative Stokes to anti-Stokes RBM Raman intensities were observed for different tubes. The bundle α in Figure 1b shows the two extreme cases. The ~199 cm⁻¹ mode appears significantly in the Stokes Raman scattering, while the 184 cm⁻¹ mode has higher anti-Stokes Raman intensity than the corresponding Stokes Raman intensity. This large variation in the RBM Stokes to anti-Stokes Raman intensity ratio is a consequence of the resonance enhancement.²⁵ These asymmetric Stokes and anti-Stokes RBM profiles have been observed²⁵ on an ensemble sample with a broad diameter distribution, but not on the ensemble sample used in the present study, which has a narrow diameter distribution. We often observed such spectra in thin bundles, demonstrating that we were indeed probing only a few individual tubes.

To obtain the relative enhancement between the RBM Stokes and anti-Stokes Raman lines, we divided the measured ratio I_s/I_{as} by²⁵

$$\alpha_{s/as} = [(\omega_L - \omega_{ph})/(\omega_L + \omega_{ph})]^4 [n(\omega_{ph}) + 1]/n(\omega_{ph}) \quad (1)$$

where ω_L and ω_{ph} are the incident laser frequency and phonon frequency, respectively, and $n(\omega_{ph})$ is the Bose–Einstein thermal factor

$$n(\omega_{ph}) = 1/[\exp(\hbar\omega_{ph}/k_B T) - 1] \quad (2)$$

The local temperature T is estimated from the peak position of the sharp ~1590 cm⁻¹ semiconducting feature²⁶ in the G-band Raman spectra. This feature downshifts with increasing temperature with a rate of ~0.043 cm⁻¹/K.²⁷ In our results, this feature, if present, shows up at ~1586 cm⁻¹ in some of the thin bundle 632 nm Raman spectra. Thus, in our case, the local temperature is ~360 K, just slightly above room temperature. The corrected ratios I_s/I_{as} , which vary because of the resonance effect, for 27 different RBM peaks observed in 18 thin bundles are plotted in Figure 2a. A wide range from ~0.2 to ~5 is observed.

The 632 nm light mostly excites metallic tubes.^{18,19} The trigonal warping effect splits the first interband optical transition, in resonance with 632 nm, into two peaks.¹³ The values of the split peaks are adopted from Saito et al.'s calculation¹³ and are plotted in Figure 2b for metallic tubes with diameters between 1.14 and 1.53 nm. Within this electronic structure model, the RBM Raman intensity is calculated using two simplified models. In general the Raman scattering cross section is proportional to the squared modulus of the Raman tensor^{11,28}

$$\mathbf{R}^{xy} = \sum_{ij} \frac{\mathbf{p}_{gi}^x \mathbf{p}_{ig}^y \Xi_{ji}}{(\omega_L - \omega_{ig})(\omega_s - \omega_{jg})} \quad (3)$$

The ω_{ig} are the energies of the resonant electronic transitions with g , i , and j labeling the ground and intermediate electronic states. \mathbf{p}_{gj}^x denotes the electron momentum matrix elements, and Ξ_{ji} refers to the electron–phonon matrix elements. If we assume the electron momentum and electron–phonon matrix elements are the same for the two components produced by trigonal splitting and assume a line width γ independent of

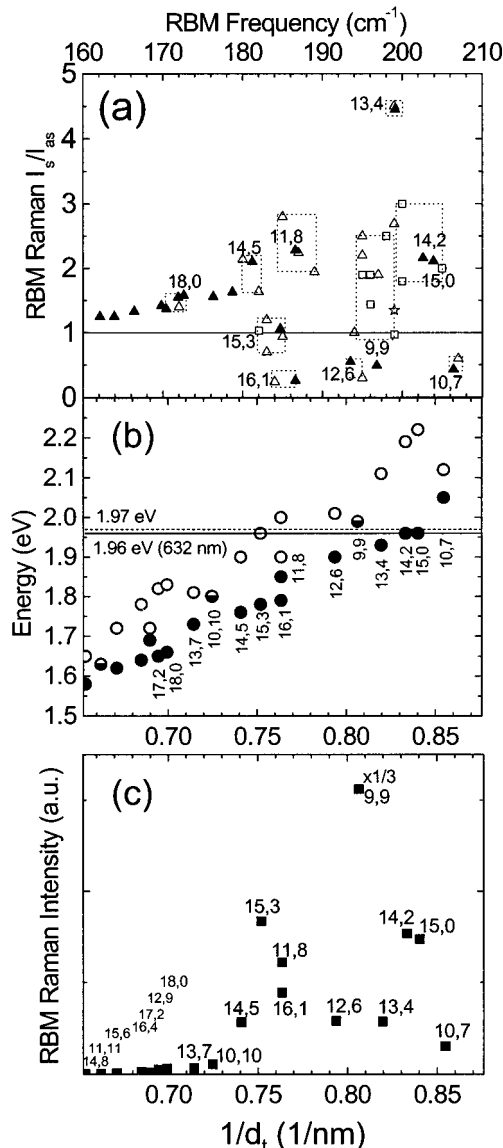


Figure 2. (a) Experimental RBM Stokes to anti-Stokes Raman intensity ratios I_s/I_{as} for 27 observed RBM peaks (Δ , \square) and calculated RBM Raman ratios I_s/I_{as} for 19 different (n, m) tubes at incidence excitation energy 1.97 eV (\blacktriangle). \square indicates intense Raman signals. The star represents I_s/I_{as} for a thick bundle. The (n, m) assignments for the observed RBM peaks are indicated by the dashed rectangles. (b) Splitting of the first interband transition $v1 \rightarrow c1$ for metallic tubes with diameters from 1.14 to 1.53 nm. The upper and lower transitions are denoted by \circ and \bullet , respectively, and the nonsplitting peaks for armchair tubes are denoted by the half filled circles. The solid and dashed horizontal lines represent $E_{\text{laser}} = 1.96$ eV and $E = 1.97$ eV used for the theoretical I_s/I_{as} data points in part a, respectively. (c) Calculated RBM Stokes Raman intensities at $E_{\text{laser}} = 1.97$ eV for the tubes in part b using the discrete model.

energy, eq 3 can be simplified to²⁹

$$\mathbf{R}^{\parallel\parallel} = \mathbf{p}^{\parallel} \mathbf{p}^{\parallel\parallel} \Xi \left(\frac{1}{\omega_L - \omega_u - i\gamma} + \frac{1}{\omega_L - \omega_l - i\gamma} \right) \left(\frac{1}{\omega_s - \omega_u - i\gamma} + \frac{1}{\omega_s - \omega_l - i\gamma} \right) \quad (4)$$

Here, two discrete trigonal resonant transitions u (upper) and l (lower) are assumed for each metallic tube (hereafter referred to as the discrete model). We have also replaced x, y with \parallel , \parallel (parallel = \parallel), because polarized Raman measurements show that scattering is strongest for (\parallel, \parallel) .^{8,19} Alternatively, if all of

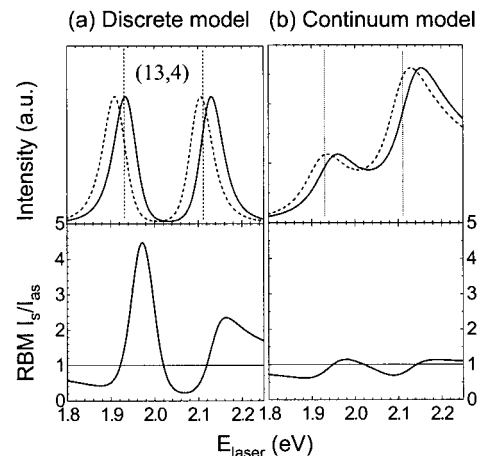


Figure 3. Calculated excitation profiles for RBM Stokes (solid line) and anti-Stokes (dashed line) Raman scattering and the Raman intensity ratio I_s/I_{as} for a (13, 4) nanotube using the discrete model (left) and the continuum model (right). Vertical dotted lines denote the two splitting electronic transitions due to the trigonal warping effect.

the resonant continuum states are included, the matrix element becomes

$$\mathbf{R}^{\parallel\parallel} = \mathbf{p}^{\parallel} \mathbf{p}^{\parallel\parallel} \Xi \left(\int \frac{\text{JDOS}(\omega)}{\omega_L - \omega - i\gamma} d\omega \right) \left(\int \frac{\text{JDOS}(\omega)}{\omega_s - \omega - i\gamma} d\omega \right) \quad (5)$$

where $\text{JDOS}(\omega)$ is the joint density of states for metallic tubes and is approximated by the sum of a pair of inverse square root functions^{26,30}

$$f(\omega) = \frac{a_0}{d_t \beta_0} \frac{\omega}{\sqrt{\omega^2 - \omega_i^2} + c}$$

Here a_0 is the C-C distance (0.144 nm), d_t is the diameter of a tube, and β_0 is the C-C nearest neighbor interaction energy (taken as 2.90 eV). ω_i is the energy position of the van Hove spikes in the DOS. The constant c is included to prevent the divergence of the function $f(\omega)$ at $\omega = \omega_i$ and is determined according to the numerical results for the DOS¹³ (hereafter referred to as the continuum model).

We find that I_s/I_{as} is very sensitive to γ in the discrete model. $\gamma = 20$ meV³¹ has been obtained previously from fitting the experimental ensemble metallic tube Raman excitation profile at 23 °C³² and is consistent with the scanning tunneling microscopy and spectroscopy (STM/STS) measurements on single tubes at 5 K.³³ If we take γ to be 20 meV, the calculated I_s/I_{as} has a maximum (minimum) of ~ 10 (~ 0.1), which is far above (below) the experimental I_s/I_{as} maximum (minimum) of ~ 5 (~ 0.2). For $\gamma = 43$ meV, the calculated I_s/I_{as} extremes are close to the experimental values. We adopt $\gamma = 43$ meV in our calculation; in the resonant Raman calculation of Richter et al.,¹¹ a γ value of 100 meV was assumed. By contrast, the continuum model calculation depends very weakly on the γ value.

The excitation profiles for I_s and I_{as} were calculated for all tubes. An example [tube (13, 4)] is shown in Figure 3 for both models. The positions of the two trigonal transitions are marked. In the discrete model, I_s/I_{as} shows an asymmetric shape, varying from ~ 0.2 to ~ 5 , depending on the incident laser excitation energy relative to the van Hove resonances. The calculated I_s/I_{as} at $E_{\text{laser}} = 1.97$ eV is shown in Figure 2a for each tube, where ω_{RBM} is calculated from diameter d_t by³⁴

$$\omega_{\text{RBM}}(d_t) = 223.75 \text{ cm}^{-1} \cdot \text{nm}/d_t + 16 \text{ cm}^{-1} \quad (6)$$

The discrete model reproduces the observed large variation in I_s/I_{as} . The continuum model gives a more symmetric profile with extremes of only ~ 0.5 to ~ 1.5 . We return to this point in a later section.

On the basis of the observed ω_{RBM} and I_s/I_{as} , we can tentatively assign an (n, m) index to the observed RBM peaks using the discrete model. In our experiment, the tubes resonantly excited by 632 nm light may have a different number of surrounding tubes in different thin bundles. This must cause some variation in ω_{RBM} for a same (n, m) tube in different thin bundles. [In Jorio et al.'s measurement,²¹ every tube has a similar environment, and they observed more uniform ω_{RBM} values.] Using eq 6, d_t corresponding to the observed ω_{RBM} frequencies in Figure 2a can be estimated to be ~ 1.17 – 1.42 nm ($1/d_t \sim 0.85$ – 0.71). This is consistent with the predicted resonant transition energies in Figure 2b. Also, there is a structural d_t gap between 1.26 and 1.31 nm ($1/d_t \sim 0.79$ – 0.76), which should lead to a gap between 187 and 193 cm^{-1} in ω_{RBM} . Figure 2a does show a gap between 189 and 194 cm^{-1} . The constant term of 16 cm^{-1} in eq 6 is adopted instead of 14 cm^{-1} to match the predicted and the observed gap. We assign the high-frequency RBM peaks ranging from 194 to 205 cm^{-1} in Figure 2a to the small diameter tubes (from (10, 7) to (12, 6)) in Figure 2b and the low-frequency RBM peaks from 172 to 189 cm^{-1} to the large diameter tubes (from (16, 1) to (18, 0)).

Our assignments are represented by the rectangles in Figure 2a. On the basis of ω_{RBM} and I_s/I_{as} , the 184 cm^{-1} peak in bundle α in Figure 1b is assigned to a (16, 1) tube, the 199 cm^{-1} feature is assigned to a (13, 4) tube, and the 185 cm^{-1} feature from bundle γ in Figure 1d is assigned to the (11, 8) structure. In the series (14, 5), (15, 3), and (16, 1), I_s/I_{as} varies from ~ 2.0 to ~ 0.25 as the upper resonance crosses the laser energy. In the series (13, 4), (14, 2), (15, 0), and (10, 7), I_s/I_{as} varies from ~ 4.5 to ~ 0.5 as the lower resonance crosses the laser energy. The relative intensity between different peaks is consistent with the calculation. For example, tubes (16, 1) and (13, 4) are predicted to have similar Stokes Raman intensities, in agreement with experiment. The (15, 3), (14, 2), and (15, 0) tubes should show relatively high Raman intensity, consistent with the observation of intense Raman signals for RBM features assigned to these tubes. Because the calculation results at $E_{laser} = 1.97$ eV better reproduce the experimental results (actually $E_{laser} = 1.96$ eV), the whole energy levels in Figure 2b, for which a carbon–carbon nearest neighbor interaction energy β_0 of 2.90 eV was used,¹³ should be lowered by 0.01 eV. That is, $\beta_0 = 2.89$ eV for best fit.

However, (9, 9) does not fit this simple model. A (9, 9) tube does not show trigonal splitting and should give by far the strongest Raman intensity, located at ~ 197 cm^{-1} . Several strong lines are indeed observed, however with $I_s/I_{as} \sim 2.0$ instead of the predicted value of 0.5. The broadened ensemble Raman signal at ~ 198 cm^{-1} exhibits $I_s/I_{as} = 1.3$ and should be dominated by (9, 9) tubes. On the basis of intensity and ω_{RBM} , (9, 9) is tentatively assigned to the data points around the ensemble one in Figure 2a, including the 196 cm^{-1} peak in bundle β in Figure 1c.

The calculation shows high sensitivity to the exact transition energy relative to E_{laser} for tubes (9, 9), (14, 2), and (15, 0). If E_{laser} is above (below) an energy level, the model predicts a Raman ratio greater (less) than 1. A large variation in Raman intensity and ratio is expected for a small energy shift in these tubes. Near resonance, our (n, m) structural assignment is limited by the accuracy of the calculated transition energies and by the assumption that all tubes have the same γ . The (9, 9) tube is

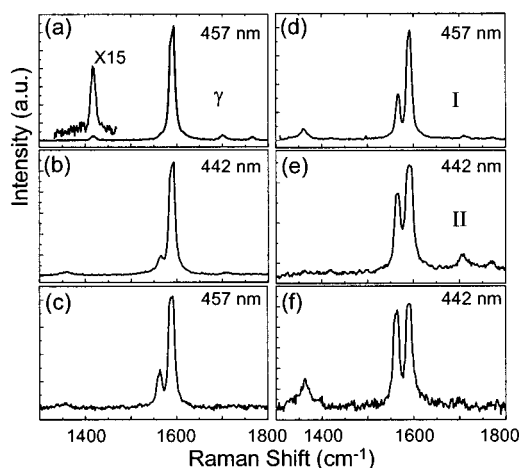


Figure 4. Raman spectra of semiconducting SWNTs in six different thin bundles (a–f) in the range 1300–1800 cm^{-1} . The excitation wavelength is 457 nm for parts a, c, and d and 442 nm for parts b, e, and f, with typical excitation intensity of 40 kW/cm^2 . Inset to part a shows the magnified view of the 1417 cm^{-1} Raman peak.

unique as two different circumferential k eigenstates yield superimposed 1D energy bands along the tube axis, within the simple tight binding model.¹³ We suggest that “solvation”³⁵ in differing small bundles lowers symmetry and splits these bands, giving a wide range of I_s/I_{as} values.

The discrete model, which ignores Raman from continuum transitions above the $c1 \rightarrow v1$ van Hove band edge, works well, indicating that the resonant window and the van Hove singularities are quite narrow. Within resonant Raman theory, this suggests that the continuum transitions have a much larger γ than the band edge transitions that give discrete states. A recent ensemble photoelectron dynamics measurement³⁶ shows that the lifetime of excited electrons decreases significantly with energy; vHs band edges were not observed. In bulk semiconductors,²⁹ and also in semiconductor nanocrystals,³⁷ a similar phenomenon occurs: resonant Raman intensity is far stronger at the band edge threshold because of a longer lifetime.

The 43 meV γ value is model dependent, and probably larger than the true value, as the discrete model ignores continuum resonance Raman scattering. A more general model might involve an energy dependent γ in the continuum model. Higher γ values may be present in our acid processed nanotubes than in as-grown CVD nanotubes, as acid processing with sonication creates some sidewall damage. The photoelectron dynamics measurement on SWNTs gave a γ value on the order of 10 meV.³⁶

Tangential G-Band Mode. Most thin bundle Raman data show both a semiconducting line shape at 457 or 442 nm excitation and a metallic line shape at 632 nm excitation. Thus, a typical thin bundle contains a few of both type tubes.

A. Semiconducting Tubes. In Figure 4 we show the G-band spectra of six different thin bundles for blue excitation. While the G-band Raman spectra of thick bundles always reproduce the ensemble spectra, quite different G-band spectra were observed in thin bundles. The spectra exhibit varying relative intensities of the 1565 cm^{-1} peak to the 1590 cm^{-1} component. Spectrum c is similar to that obtained from an ensemble sample. From spectrum a to spectrum f, the 1565 cm^{-1} peak intensity increases relative to the 1590 cm^{-1} peak. In spectrum a only the 1590 cm^{-1} peak shows up, while in spectrum f both 1565 and 1590 cm^{-1} components have identical intensities.

Group theory predicts that six Raman-active modes can be present in the G-band for a general chiral SWNT: two A_1 (A_{1g}),

two E_1 (E_{1g}), and two E_2 (E_{2g}) modes.^{1,6} For each symmetry mode, the atomic vibrations can be along the tube axis (LO) or along the circumferential direction (TO).^{8–10} For zigzag and armchair tubes (both are achiral, symmorphic groups), only three modes are Raman active in the G-band: A_{1g} , E_{1g} , and E_{2g} . The resonant spectra are dominated by A_1 (A_{1g}) modes, in both simple theory¹¹ and polarized Raman measurements.⁸ Our 457 or 442 nm laser is polarized along the tube axis, and we expect the observed peaks are A_{1g} modes. The lower frequency 1565 cm^{-1} is assigned to circumferential vibration (with a lower force constant); the 1590 cm^{-1} peak is assigned to axial vibration (with a higher force constant).

The relative intensities of the two peaks are predicted to depend on chirality.^{8–10} The 1590 cm^{-1} feature comes from low chiral angle tubes, while the 1565 cm^{-1} peak is dominated by high chiral angle tubes. Also, the single A_{1g} mode vibration in an armchair tube, along the circumferential direction, occurs at 1565 cm^{-1} , while in a zigzag tube, this A_{1g} axial mode is at 1590 cm^{-1} . (A zigzag tube has the smallest chiral angle of 0°, and an armchair tube has the largest chiral angle of 30°.) Our data in Figure 4 strongly support the predicted chirality dependence of G-band Raman scattering in SWNTs, although we do not have an independent chirality determination. Bundle γ in Figure 4a shows only the 1590 cm^{-1} peak, as expected for zigzag tubes. From spectrum b to spectrum f the 1565 cm^{-1} peak increases relative to the 1590 cm^{-1} peak, implying that high chiral angle tubes begin to be present with increasing degree.

The data in Figure 4 have not been observed in prior ensemble or single tube experiments. Odom et al. studied the chiral angle distribution of tubes in thick bundles and etched thin bundles with scanning tunneling microscopy (STM).³⁸ In thick bundles, the chiral angle distribution is favored toward zigzag tubes, while thin bundles exhibit a random distribution. This may explain why the thick bundle Raman spectra^{8,18,19} always look like that in Figure 4c. They also found that if a bundle is perfectly and closely packed, the tubes tend to have a similar chirality; Figure 4 supports this conclusion. Depolarization or an *antenna* effect in carbon nanotubes may also explain the ensemble Raman spectra, as discussed by Saito et al.¹⁰

Bundle γ in Figure 4a shows a weak feature at 1417 cm^{-1} . This feature is not the disorder-induced D-band, which appears at ~ 1370 cm^{-1} for 457 nm excitation. Kasuya et al.³⁹ suggested that modes between 1300 and 1500 cm^{-1} are sensitive to chirality. Theoretical calculations also show the presence of 1300–1500 cm^{-1} modes only in achiral tubes.⁴⁰ Such modes have not been reported. The 1417 cm^{-1} feature clearly shown in Figure 4a, we believe, is one of these modes, and it supports the existence of mainly zigzag semiconducting tubes in this bundle γ . On the basis of the strong Raman intensity, the semiconducting tubes in bundle γ are assigned to (17, 0) structures, which have $E_{33}^s \sim 2.62$ eV and $E_{44}^s \sim 2.77$ eV,¹³ close to $E_{\text{laser}} = 2.71$ eV and $E_{\text{scatter}} = 2.51$ eV. Another feature for this specific thin bundle was observed at ~ 1015 cm^{-1} . As shown below, the 632 nm Raman scattering of bundle γ shows weak metallic Raman intensity compared with the 457 nm Raman scattering. Also, a relatively strong semiconducting feature at 1587 cm^{-1} is observed in the 632 nm G-band Raman, suggesting the dominance of semiconducting tubes in bundle γ , consistent with the observation of strong 457 nm Raman scattering.

Because all the armchair tubes are metallic and not resonantly selected by 457 or 442 nm excitation, we would not expect to observe a G-band Raman spectrum showing only the lower

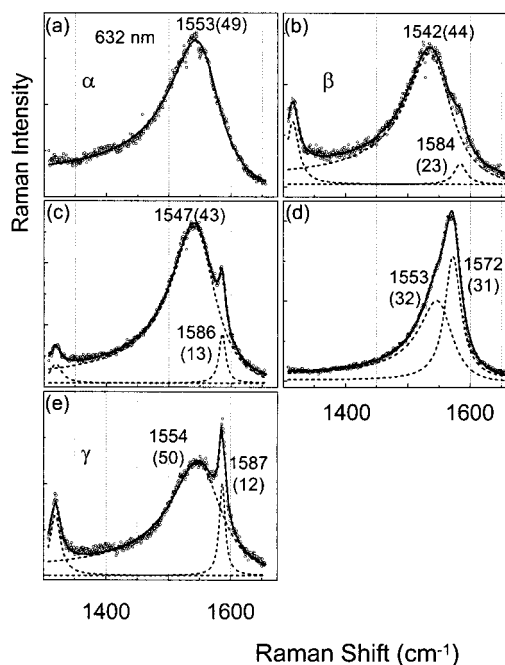


Figure 5. Raman spectra of five different thin bundles of SWNTs (a–e) in the range 1300–1650 cm^{-1} with 632 nm excitation. The excitation intensities are 110 kW/cm^2 for parts a, and d and 220 kW/cm^2 for parts b, c, and e. The numbers in the figure indicate the fitted peak positions (widths) in inverse centimeters.

frequency 1565 cm^{-1} peak from armchair tubes with 457 or 442 nm excitation.

B. Metallic Tubes. In Figure 5 are shown the G-band Raman spectra from five thin bundles with 632 nm excitation; similar changes in relative intensities occur as in Figure 4.

The ensemble 632 nm spectra show complex features,^{5,32} with a broad Fano Raman line⁷ at ~ 1540 cm^{-1} assigned by Brown et al. to the coupling of the 1565 cm^{-1} A_{1g} mode with continuum electronic π plasmon excitation.⁹ Brown et al. have observed simpler G-band Raman spectra from metallic tubes at the anti-Stokes side,⁴¹ which empirically are fit by a Fano line shape function at ~ 1540 cm^{-1} and a Lorentzian function at ~ 1580 cm^{-1} .⁹ We observe similar simple spectra for thin bundles on the Stokes side, which also can be fit by a Fano line shape function and a Lorentzian function, with varying relative intensities. The Fano peaks range from ~ 1542 to ~ 1553 cm^{-1} ; the variation can be due to the temperature, gas adsorption effect,^{18,19} or different tube diameters.⁹ The 1572 cm^{-1} peak in Figure 5d is attributed to metallic tubes, similar to the ~ 1580 cm^{-1} peak observed before.^{9,20} The sharper 1586 and 1587 cm^{-1} peaks are assigned to nonresonantly excited semiconducting tubes (see below). They are downshifted from 1590 cm^{-1} because of the laser heating effect.²⁷

The same chirality dependence of G-band Raman scattering discussed above for semiconducting tubes, in principle, should apply to metallic tubes. Figure 5 indicates the evidence for this chirality dependence, although possibly more than one tube can contribute to the spectra. The bundle α in Figure 5a shows only the Fano peak and may contain only higher chiral angle metallic tubes. Figure 5d exhibits both a Fano peak and a stronger Lorentzian peak, suggesting the dominance of the lower chiral angle metallic tubes in the bundle. The characteristic Raman features between 1300 and 1500 cm^{-1} for achiral tubes are probably too weak to be observed on the long Fano peak tail in Figure 5a.

However, the RBM features of bundle α have been assigned to (16, 1) and (13, 4) tubes, neither of which are high chiral

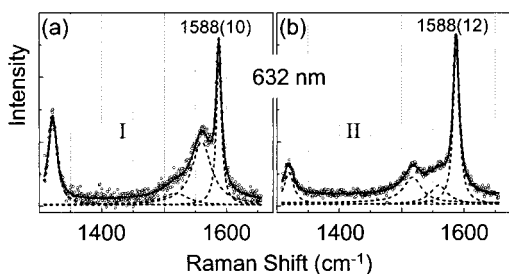


Figure 6. Raman spectra of two different thin bundles, I and II, of SWNTs in the range 1300–1650 cm^{-1} with 632 nm excitation at 220 kW/cm^2 . Note the strong, sharp peak at 1588 cm^{-1} . The frequencies (widths) are displayed.

angle metallic tubes, as inferred from the G-band Raman spectrum for this bundle. Thus, the chirality information for tubes from the RBM Raman ratio seems inconsistent with that from the G-band Raman spectrum. This implies that more than one (at least three) metallic tubes are present in the bundle α . As shown by Richter et al.,¹¹ a nanotube exhibits different RBM and G-band Raman excitation profiles. Thus, different tubes might contribute to the RBM and G-band Raman scattering. A Raman scattering measurement on the same tube is needed to further address the problem of the chirality dependence of Raman scattering from SWNTs.

All ~ 20 thin bundles studied show the broad Fano Raman line at $\sim 1540 \text{ cm}^{-1}$ with 632 nm excitation, except bundles I and II in Figure 6. Thus, we believe that the Fano Raman resonance is an intrinsic property of metallic tubes. In ensemble spectra with 632 nm excitation, a sharp feature at $\sim 1590 \text{ cm}^{-1}$ always occurs.³² This peak has been assumed to come from semiconducting tubes,³² and it has been proven by measuring an excitation profile on the ensemble sample.²⁶ In thin bundles I and II, we observed a strong $\sim 1588 \text{ cm}^{-1}$ feature with 632 nm excitation, as shown in Figure 6. These spectra are similar to the typical semiconducting Raman spectra with 457 nm excitation shown in Figure 4c. The observation of only the Fano peak in one bundle (Figure 5a) and mainly the strong 1588 cm^{-1} peak in another bundle (Figure 6), both with 632 nm excitation, indicates that these lines do not belong to the same tube. The spectra in Figures 5 and 6 are all simpler than the ensemble spectra. Thus, our results help interpret the complex ensemble spectra.

Conclusion

In summary, Raman spectra obtained on single SWNTs in thin bundles exhibit different and new features compared to those of the ensemble spectra. First, a large variation in the I_s/I_{as} was observed. A simplified resonance Raman calculation reproduces the observed ratio well, with the exception of that for (9, 9), thus supporting the existence of the trigonal warping splitting and the chirality dependence of the electronic structure of SWNTs. Second, the observed variation of the G-band Raman spectra from thin bundles provides strong evidence for the chirality dependence of Raman scattering intensity in SWNTs. Our results also help to explain the complex Raman spectra on ensemble samples. We did not correlate the RBM Raman scattering with the G-band Raman scattering for a same thin bundle. Further studies, both Raman measurement and chirality determination on individual tubes, are needed to address the chirality dependence and other properties of electronic structure and vibrational modes in SWNTs.

It is promising that Raman scattering may provide an unambiguous, convenient, and noninvasive way to determine

(n , m), on the basis of the relative G-band Raman intensity, RBM frequency, and I_s/I_{as} . This is especially important for encapsulated (insulated) SWNTs, where the surface is not available for local probe examination.

Acknowledgment. We thank Min Zhu and Lian Ouyang for discussions and suggestions. We also thank M. Dresselhaus, G. Dresselhaus, and R. Saito for informative correspondence and preprints of refs 9, 10, and 21. We are very grateful to R. Saito for providing the data used in Figure 2b. This work was supported by the DOE under Contract FG02-98ER14861 and has benefited from materials characterization facilities at Columbia supported by MRSEC Grant DMR-98-09687.

References and Notes

- (1) Dresselhaus, M. S.; Dresselhaus, G.; Eklund, P. C. *Science of Fullerenes and Carbon Nanotubes*; Academic Press: New York, 1996.
- (2) Saito, R.; Dresselhaus, G.; Dresselhaus, M. S. *Physical Properties of Carbon Nanotubes*; Imperial College Press: London, 1998.
- (3) Iijima, S.; Ichihashi, T. *Nature* **1993**, *363*, 603.
- (4) Bethune, D. S.; Chiang, C. H.; Vries, M. S. d.; Gorman, G.; Savoy, R.; Vazquez, J.; Beyers, R. *Nature* **1993**, *363*, 605.
- (5) Rao, A. M.; Richter, E.; Bandow, S.; Chase, B.; Eklund, P. C.; Williams, K. A.; Fang, S.; Subbaswamy, K. R.; Menon, M.; Thess, A.; Smalley, R. E.; Dresselhaus, G.; Dresselhaus, M. S. *Science* **1997**, *275*, 187.
- (6) Saito, R.; Takeya, T.; Kimura, T.; Dresselhaus, G.; Dresselhaus, M. S. *Phys. Rev. B* **1998**, *57*, 4145.
- (7) Kataura, H.; Kumazawa, Y.; Maniwa, Y.; Umezumi, I.; Suzuki, S.; Ohtsuka, Y.; Achiba, Y. *Synth. Met.* **1999**, *103*, 2555.
- (8) Jorio, A.; Dresselhaus, G.; Dresselhaus, M. S.; Souza, M.; Dantas, M. S. S.; Pimenta, M. A.; Rao, A. M.; Saito, R.; Liu, C.; Cheng, H. M. *Phys. Rev. Lett.* **2000**, *85*, 2617.
- (9) Brown, S. D. M.; Jorio, A.; Corio, P.; Dresselhaus, M. S.; Dresselhaus, G.; Saito, R.; Kneipp, K. *Phys. Rev. B* **2001**, *63*, 155414.
- (10) Saito, R.; Jorio, A.; Hafner, J. H.; Lieber, C. M.; Hunter, M.; McClure, T.; Dresselhaus, G.; Dresselhaus, M. S. *Phys. Rev. B*, submitted for publication.
- (11) Richter, E.; Subbaswamy, K. R. *Phys. Rev. Lett.* **1997**, *79*, 2738.
- (12) Charlier, J. C.; Lambin, P. *Phys. Rev. B* **1998**, *57*, R15037.
- (13) Saito, R.; Dresselhaus, G.; Dresselhaus, M. S. *Phys. Rev. B* **2000**, *61*, 2981.
- (14) Friedman, J.; Hochstrasser, R. M. *Chem. Phys. Lett.* **1975**, *32*, 414.
- (15) Mortensen, O. S.; Hassing, S. Polarization and Interference Phenomena in Resonance Raman Scattering. In *Advances in Infrared and Raman Spectroscopy*; Clark, R. J. H., Hester, R. E., Eds.; Heyden: London, 1980; Vol. 6.
- (16) Rao, A. M.; Bandow, S.; Richter, E.; Eklund, P. C. *Thin Solid Films* **1998**, *331*, 141.
- (17) Pimenta, M. A.; Marucci, A.; Brown, S. D. M.; Matthews, M. J.; Rao, A. M.; Eklund, P. C.; Smalley, R. E.; Dresselhaus, G.; Dresselhaus, M. S. *J. Mater. Res.* **1998**, *13*, 2396.
- (18) Yu, Z.; Brus, L. E. *J. Phys. Chem. A* **2000**, *104*, 10995.
- (19) Yu, Z.; Brus, L. *J. Phys. Chem. B* **2001**, *105*, 1123.
- (20) Duesberg, G. S.; Loa, I.; Burghard, M.; Syassen, K.; Roth, S. *Phys. Rev. Lett.* **2000**, *85*, 5436.
- (21) Jorio, A.; Saito, R.; Hafner, J.; Lieber, C. M.; Dresselhaus, G.; Dresselhaus, M. S. *Phys. Rev. Lett.* **2001**, *86*, 1118.
- (22) Rinzler, A. G.; Liu, J.; Dai, H.; Nikolaev, P.; Huffman, C. B.; Rodriguez-Macias, F. J.; Boul, P. J.; Lu, A. H.; Heymann, D.; Colbert, D. J.; Lee, R. S.; Fischer, J. E.; Rao, A. M.; Eklund, P. C.; Smalley, R. E. *Appl. Phys. A* **1998**, *67*, 29.
- (23) Duesberg, G. S.; Blau, W. J.; Byrne, H. J.; Muster, J.; Burghard, M.; Roth, S. *Chem. Phys. Lett.* **1999**, *310*, 8.
- (24) Thess, A.; Lee, R.; Nikolaev, P.; Dai, H. J.; Petit, P.; Robert, J.; Xu, C. H.; Lee, Y. H.; Kim, S. G.; Rinzler, A. G.; Colbert, D. T.; Scuseria, G. E.; Tomanek, D.; Fischer, J. E.; Smalley, R. E. *Science* **1996**, *273*, 483.
- (25) Tan, P. H.; Tang, Y.; Hu, C. Y.; Li, F.; Wei, Y. L.; Cheng, H. M. *Phys. Rev. B* **2000**, *62*, 5186.
- (26) Rafailov, P. M.; Jantoljak, H.; Thomsen, C. *Phys. Rev. B* **2000**, *61*, 16179.
- (27) Li, H. D.; Yue, K. T.; Lian, Z. L.; Zhan, Y.; Zhou, L. X.; Zhang, S. L.; Shi, Z. J.; Gu, Z. N.; Liu, B. B.; Yang, R. S.; Yang, H. B.; Zou, G. T.; Zhang, Y.; Iijima, S. *Appl. Phys. Lett.* **2000**, *76*, 2053.
- (28) Hayes, W.; Loudon, R. *The Scattering of Light by Crystals*; John Wiley: New York, 1976.
- (29) Martin, R. M.; Falicov, L. M. Resonant Raman Scattering. In *Light Scattering in Solids*; Cardona, M., Ed.; Springer-Verlag: New York, 1975.

- (30) Mintmire, J. W.; White, C. T. *Phys. Rev. Lett.* **1998**, *81*, 2506.
- (31) The definition of the line width parameter used in ref 28 differs from ours by a factor of 2.
- (32) Pimenta, M. A.; Marucci, A.; Empedocles, S. A.; Bawendi, M. G.; Hanlon, E. B.; Rao, A. M.; Eklund, P. C.; Smalley, R. E.; Dresselhaus, G.; Dresselhaus, M. S. *Phys. Rev. B* **1998**, *58*, R16016.
- (33) Wildöer, J. W. G.; Venema, L. C.; Rinzler, A. G.; Smalley, R. E.; Dekker, C. *Nature* **1998**, *391*, 59.
- (34) Venkateswaran, U. D.; Rao, A. M.; Richter, E.; Menon, M.; Rinzler, A.; Smalley, R. E.; Eklund, P. C. *Phys. Rev. B* **1999**, *59*, 10928.
- (35) Kwon, Y.-K.; Saito, S.; Tománek, D. *Phys. Rev. B* **1998**, *58*, R13314.
- (36) Hertel, T.; Moos, G. *Chem. Phys. Lett.* **2000**, 320, 359.
- (37) Alivisatos, A. P.; Harris, T. D.; Carroll, P. J.; Steigerwald, M. L.; Brus, L. E. *J. Chem. Phys.* **1989**, *90*, 3463.
- (38) Odom, T. W.; Huang, J. L.; Kim, P.; Lieber, C. M. *J. Phys. Chem. B* **2000**, *104*, 2794.
- (39) Kasuya, A.; Sasaki, Y.; Saito, Y.; Tohji, K.; Nishina, Y. *Phys. Rev. Lett.* **1997**, *78*, 4434.
- (40) Eklund, P. C.; Holden, J. M.; Jishi, R. A. *Carbon* **1995**, *33*, 959.
- (41) Brown, S. D. M.; Corio, P.; Marucci, A.; Dresselhaus, M. S.; Pimenta, M. A.; Kneipp, K. *Phys. Rev. B* **2000**, *61*, R5137.